

**Elastic theory of origami-based metamaterials**V. Brunck,<sup>1</sup> F. Lechenault,<sup>1</sup> A. Reid,<sup>1,2</sup> and M. Adda-Bedia<sup>1</sup><sup>1</sup>*Laboratoire de Physique Statistique, Ecole Normale Supérieure, UPMC Université Paris 06, Université Paris-Diderot, CNRS, 24 rue Lhomond 75005 Paris, France*<sup>2</sup>*Department of Physics, North Carolina State University, North Carolina 27695, USA*

(Received 16 July 2015; revised manuscript received 8 January 2016; published 22 March 2016)

Origami offers the possibility for new metamaterials whose overall mechanical properties can be programmed by acting locally on each crease. Starting from a thin plate and having knowledge about the properties of the material and the folding procedure, one would like to determine the shape taken by the structure at rest and its mechanical response. In this article, we introduce a vector deformation field acting on the imprinted network of creases that allows us to express the geometrical constraints of rigid origami structures in a simple and systematic way. This formalism is then used to write a general covariant expression of the elastic energy of  $n$ -creases meeting at a single vertex. Computations of the equilibrium states are then carried out explicitly in two special cases: the generalized waterbomb base and the Miura-Ori. For the waterbomb, we show a generic bistability for any number of creases. For the Miura folding, however, we uncover a phase transition from monostable to bistable states that explains the efficient deployability of this structure for a given range of geometrical and mechanical parameters. Moreover, the analysis shows that geometric frustration induces residual stresses in origami structures that should be taken into account in determining their mechanical response. This formalism can be extended to a general crease network, ordered or otherwise, and so opens new perspectives for the mechanics and the physics of origami-based metamaterials.

DOI: [10.1103/PhysRevE.93.033005](https://doi.org/10.1103/PhysRevE.93.033005)**I. INTRODUCTION**

Since the mid-1980s, the ancient art of paper folding has evolved into a fertile scientific field gathering distant disciplines. Using the mathematics of flat foldability [1,2], computational origami has made possible the creation of an enormous amount of new designs. The interest has also switched from the depiction of concrete objects like the traditional cranes of Japan's Edo period to abstract structures like tessellations, whose strange mechanical properties have aroused the curiosity of engineers and physicists alike. Origami metamaterials display, for example, auxetic behavior [3,4] and multistability [5–7], the latter allowing reprogrammable reconfigurations [8].

Ubiquitous in nature where permanent creases can form as a result of growth in a constraining container (e.g., dragonfly wings [9] and petal leaves [10,11]), origami structures are also well represented in domains where strength or deployable properties are attractive benefits, be it in fashion [12,13], architecture [14], medicine [15], or engineering, from airbags to consumer electronics to deployable space structures [16–20]. In all these areas, a question of paramount importance is how a particular crease affects the shape and mechanical properties of the overall structure.

To answer this question the folds are usually modeled by elastic hinges of specific stiffnesses and rest angles. In this approach, each crease lies at the intersection between two panels, whose response is governed by a length scale  $L^*$  that controls whether the panels actually bend or fold [21,22]. More precisely, this *origami length*  $L^* = B/\kappa$  is the ratio between the bending modulus  $B$  of the faces and the torsional stiffness  $\kappa$  of the crease. When the typical length of the panels is small compared to  $L^*$ , the system behaves as a rigid origami, with faces remaining mostly undeformed and creases actuating when submitted to stress. On the other hand, if the faces typical

size is larger than  $L^*$ , then the mechanical response will be governed by the bending of the sheet, while the angles of the creases will essentially keep their rest value [7]. The existence of the length scale  $L^*$  restricts the apparent scalability of origami structures. Nevertheless, we look in the following at the realm of rigid origami, which corresponds to taking systems with infinitely rigid faces and flexible creases.

The process of making an origami structure consists in printing a given planar graph on a flat sheet, which defines the reference state, and then applying a plastic deformation to this network that assigns to each edge a given stiffness and rest angle. The three-dimensional shape taken by the structure is a minimizer of the mechanical energy subject to kinematic constraints. For this purpose, the first step is to consider a single vertex with  $n$  creases coming out of it, which constitutes the building block of any origami tessellation. In the case of rigid origami, the standard approach is to find the energy minimum of such a vertex by summing over the creases, each one having different stiffness  $\kappa_i$  and rest crease angle  $\psi_i^0$ :  $E_h = \sum_{i=1}^n \kappa_i (\psi_i - \psi_i^0)^2 / 2$ , where  $\psi_i$  is the opening angle of the  $i$ th fold [4,5]. This energy must be supplemented by the geometrical constraints that the faces remain rigid during deformation. However, in many practical applications these constraints are not explicitly given in terms of the folds angles  $\psi_i$ , which forces us to adapt the energy minimization procedure for each study. This approach is thus not convenient for building a general framework for the elasticity of origami structures.

Here we provide a description of origami tessellations by expressing the deformation in terms of the vectors carried by the crease network instead of the folds angles. This approach offers us the possibility to take into account the geometric frustration using the same field of vectors, which renders energy minimization systematic and straightforward. Because origami can be seen as a three-dimensional deformation of

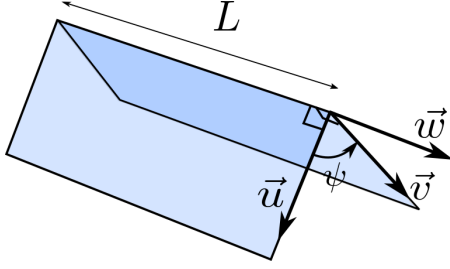


FIG. 1. The geometry of a single straight crease can be described by its length  $L$  and the three unit vectors  $(\vec{u}, \vec{v}, \vec{w})$ .

an initially flat planar graph, the vector field carried by the crease network is a natural measure of the deformation of such folded structures that allows for studying complex origami designs [23] and models of crumpled paper [24].

After detailing our approach, we apply it to two special cases that have the advantage of exhibiting a single degree of freedom: the generalized waterbomb base and the Miura-Ori. These are well studied systems allowing for comparison to existing literature. By displaying applications of our description, we hope to convey its ability to solve a vast array of problems in rigid origami by applying a simple and systematic procedure.

## II. EQUILIBRIUM STATE OF A SINGLE CREASE

We begin by considering a single straight crease of length  $L$ , that we simply model by the intersection of two rigid planar panels. The geometry of the crease and the faces can then be described by three unit vectors (Fig. 1):  $(\vec{u}, \vec{w})$  for the first plane and  $(\vec{v}, \vec{w})$  for the second one, such that  $\vec{u} \cdot \vec{w} = \vec{v} \cdot \vec{w} = 0$  and  $\vec{w}$  lies along the crease.

Let us compute the elastic energy per unit length  $\mathcal{E}$  stored in the crease. Being a scalar invariant quantity,  $\mathcal{E}$  is a linear combination of the invariants built from the set of vectors describing the geometry of the system. Here the only nonvanishing quantities are the scalar product  $\vec{u} \cdot \vec{v}$  and the triple product  $(\vec{u} \times \vec{v}) \cdot \vec{w}$ . However, the latter term is a scalar if  $\vec{w}$  is a pseudovector (since  $\vec{u} \times \vec{v}$  is a pseudovector). Therefore,  $\vec{w}$  should be written as

$$\vec{w} = \frac{\vec{u} \times \vec{v}}{|\vec{u} \times \vec{v}|}. \quad (1)$$

The leading order contributions to the elastic energy of the crease are then given by:

$$E = L \mathcal{E}(\vec{u}, \vec{v}, \vec{w}) = L (\lambda \vec{u} \cdot \vec{v} + \mu (\vec{u} \times \vec{v}) \cdot \vec{w}), \quad (2)$$

where  $\lambda$  and  $\mu$  are material real constants. Note that Eq. (1) ensures that the crease energy (2) is invariant under the transformation  $\vec{u} \leftrightarrow \vec{v}$ . With the notations of Fig. 1, one has  $\vec{u} \cdot \vec{v} = \cos \psi$  and  $(\vec{u} \times \vec{v}) \cdot \vec{w} = |\sin \psi|$ . We then introduce  $\kappa$  and  $\psi_0 \in [0, \pi]$ , such that

$$\lambda = -\kappa \cos \psi_0, \quad \mu = -\kappa \sin \psi_0, \quad (3)$$

allowing us to rewrite Eq. (2) as

$$E = \begin{cases} -L \kappa \cos(\psi - \psi_0) & \text{for } 0 \leq \psi \leq \pi \\ -L \kappa \cos(\psi + \psi_0) & \text{for } \pi \leq \psi \leq 2\pi \end{cases}. \quad (4)$$

For  $\psi \approx \psi_0$ , one recovers the usual energy of an elastic hinge [4–7,22]

$$E_h = \frac{1}{2} L \kappa (\psi - \psi_0)^2 + E_0, \quad (5)$$

where  $E_0$  is a constant,  $\kappa$  is the stiffness, and  $\psi_0$  is the rest angle of the crease (the angle in the absence of external loading [21,22]). The quadratic expression of the energy (5) sets the physical meaning of the constants  $\lambda$  and  $\mu$  through Eq. (3) and shows that the covariant energy (2) does not introduce additional material parameters.

Equation (4) shows that the energy landscape is even with respect to  $\psi = \pi$  and is cusped at that location for all  $\psi_0 \neq 0$ . Moreover, two equilibrium configurations are possible for  $\psi \in [0, 2\pi]$ ,

$$\psi \equiv \psi_m = \psi_0 \quad \text{and} \quad \psi \equiv \psi_v = 2\pi - \psi_0. \quad (6)$$

However, the result  $\psi_v = 2\pi - \psi_m$  indicates that these two solutions correspond to the same state of the crease but “observed” from the two different sides of the folded sheet. Therefore, expressing the energy of the crease in terms of the vectors associated with the faces allows us to capture the mirror-symmetry without enforcing it. The combination of this result with the cusp in the energy at  $\psi = \pi$  restricts the crease equilibrium angle  $\psi_m$  (respectively,  $\psi_v$ ) to vary in the interval  $[0, \pi]$  (respectively,  $[\pi, 2\pi]$ ). This physically based limiting angle variation is in agreement with the behavior of creased sheets in real materials.

For a single fold, the crease energy as given by Eq. (5) is reasonable for several applications [22,25]. However, we show in the following that for the case of interacting creases the parametrization of the crease energy in terms of the vectors  $(\vec{u}, \vec{v}, \vec{w})$  becomes relevant. Finally, notice that such parametrization is not unique, and, instead, one could use the unit vectors  $(\vec{n}_u, \vec{n}_v, \vec{w})$ , where  $(\vec{n}_u, \vec{n}_v)$  are the normals to the faces, and retrieve Eq. (4). Nevertheless, starting from Eq. (2) allows us to set a general framework for the elasticity of origami designs.

## III. ENERGY OF A SINGLE VERTEX

We now extend our approach to determine the energy of a vertex with  $n$ -creases of possibly different lengths  $L_i$  (Fig. 2). Because every origami network, ordered or otherwise, can be decomposed into a collection of such vertices, this structure

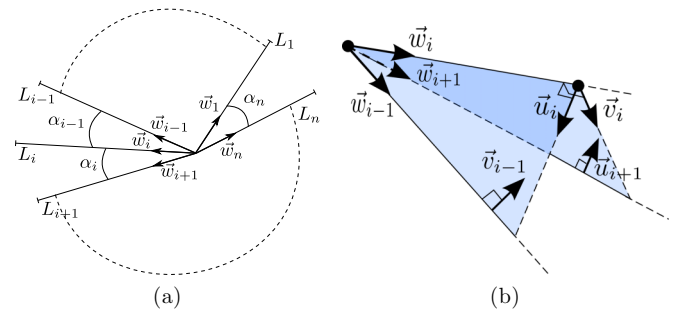


FIG. 2.  $n$ -creases meeting at a single vertex. (a) The imprinted pattern of creases is described by their lengths  $L_i$  and unit vectors  $\vec{w}_i$  separated by angles  $\alpha_i$  ( $i = 1, \dots, n$ ). (b) A subset of three adjacent creases after deformation.

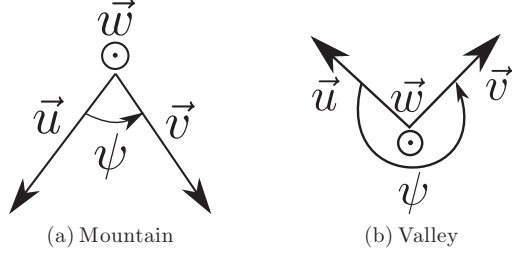


FIG. 3. Definition of mountain and valley creases.

constitutes the building block of any rigid origami design. For each crease, we define the unit vector  $\vec{w}_i$ , taken along the  $i$ th crease and pointing outward from the vertex, and the unit vectors  $\vec{u}_i, \vec{v}_i$  (see Fig. 2). We also introduce for each crease the material constants:

$$\lambda_i = -\kappa_i \cos \psi_i^0, \quad \mu_i = -\kappa_i \sin \psi_i^0, \quad (7)$$

with  $\kappa_i$  and  $\psi_i^0$  the stiffness and rest angle of the  $i$ th crease as imposed by the operator when machining the structure. Let  $\alpha_i$  be the angle between  $\vec{w}_i$  and  $\vec{w}_{i+1}$ , with  $\sum_{i=1}^n \alpha_i = 2\pi$ , and use the periodic convention  $\vec{w}_{i+n} \equiv \vec{w}_i$ . Because we consider the rigid face limit, this angle remains constant during the deformation of the sheet from its initial flat state to the folded one. We then have  $n$  constraints given by:

$$C_i = \vec{w}_i \cdot \vec{w}_{i+1} - \cos \alpha_i = 0, \quad i = 1, \dots, n. \quad (8)$$

As there is no interaction between the folds apart from the geometrical constraints, the energy of the vertex is obtained by summing over all creases,

$$E = \sum_{i=1}^n L_i [\lambda_i \vec{u}_i \cdot \vec{v}_i + \mu_i (\vec{u}_i \times \vec{v}_i) \cdot \vec{w}_i]. \quad (9)$$

Note that the directions of  $\vec{w}_i$  are fixed independently of the directions of  $\vec{u}_i$  and  $\vec{v}_i$  (see Fig. 2). Thus one has  $(\vec{u}_i \times \vec{v}_i) \cdot \vec{w}_i = \sin \psi_i$ , where the crease angle  $\psi_i$  is now defined as the oriented angle  $(\vec{u}_i, \vec{v}_i)$ . This writing does not modify the results of Sec. II and allows us to introduce the so-called mountain and valley creases (see Fig. 3).

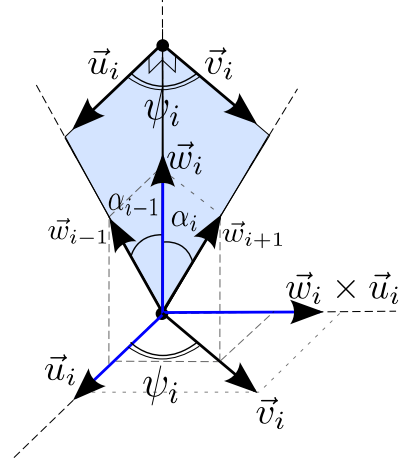
Figure 2(b) shows that each panel contains four vectors. For example, the left panel in Fig. 2(b) contains  $(\vec{w}_{i-1}, \vec{w}_i, \vec{v}_{i-1}, \vec{u}_i)$ , whereas the right panel contains  $(\vec{w}_{i+1}, \vec{w}_i, \vec{v}_i, \vec{u}_{i+1})$ . Since two vectors are sufficient to define each plane, one can write two vectors as a combination of the two others. Therefore there exists a decomposition of  $\vec{u}_i$  and  $\vec{v}_i$  in terms of  $(\vec{w}_{i-1}, \vec{w}_i, \vec{w}_{i+1})$ , so we can rewrite Eq. (9) using the crease vectors  $\vec{w}_i$  only.

A simple and visual way to find such a decomposition is to use the orthonormal base  $(\vec{u}_i, \vec{w}_i \wedge \vec{u}_i, \vec{w}_i)$  (Fig. 4), in which one has

$$\vec{v}_i = (\cos \psi_i, \sin \psi_i, 0), \quad (10)$$

$$\vec{w}_{i-1} = (\sin \alpha_{i-1}, 0, \cos \alpha_{i-1}), \quad (11)$$

$$\vec{w}_{i+1} = (\sin \alpha_i \cos \psi_i, \sin \alpha_i \sin \psi_i, \cos \alpha_i). \quad (12)$$

FIG. 4. The projections of the vectors  $\vec{v}_i, \vec{w}_{i-1}$ , and  $\vec{w}_{i+1}$  in the orthonormal base  $(\vec{u}_i, \vec{w}_i \wedge \vec{u}_i, \vec{w}_i)$ .

Then one can show that

$$\vec{u}_i \cdot \vec{v}_i = \frac{\vec{w}_{i-1} \cdot \vec{w}_{i+1} - \cos \alpha_{i-1} \cos \alpha_i}{\sin \alpha_{i-1} \sin \alpha_i}, \quad (13)$$

$$(\vec{u}_i \times \vec{v}_i) \cdot \vec{w}_i = \frac{(\vec{w}_{i-1} \times \vec{w}_{i+1}) \cdot \vec{w}_i}{\sin \alpha_{i-1} \sin \alpha_i}. \quad (14)$$

Using this result, one finds that Eq. (9) is transformed into:

$$E = \sum_{i=1}^n \tilde{L}_i [\lambda_i \vec{w}_{i-1} \cdot \vec{w}_{i+1} + \mu_i (\vec{w}_{i-1} \times \vec{w}_{i+1}) \cdot \vec{w}_i], \quad (15)$$

where a constant term has been discarded (the  $\alpha_i$ 's being fixed) and

$$\tilde{L}_i = \frac{L_i}{\sin \alpha_i \sin \alpha_{i-1}} \quad (16)$$

is an effective length of the  $i$ th crease.

The elastic energy of the vertex is expressed only in terms of the field  $\vec{w}_i$  that completely describes the deformation of the crease network. Moreover, the geometric constraints (8) and the conditions  $|\vec{w}_i|^2 = 1$  are also given in terms of the same field of vectors. Therefore, the equilibrium configuration of the vertex can be determined by minimizing the following energy functional:

$$E^* = E - \sum_{i=1}^n \gamma_i C_i - \sum_{i=1}^n \delta_i (|\vec{w}_i|^2 - 1), \quad (17)$$

where  $\gamma_i$  and  $\delta_i$  are Lagrange multipliers. The minimization with respect to the components of the vectors  $\vec{w}_i, \gamma_i$ , and  $\delta_i$  yields a closed system of  $5n$  equations. The crease angles  $\psi_i$  can be derived *a posteriori* from the vector field  $\vec{w}_i$  using [see Eq. (13)]

$$\cos \psi_i = \frac{\vec{w}_{i-1} \cdot \vec{w}_{i+1} - \cos \alpha_{i-1} \cos \alpha_i}{\sin \alpha_{i-1} \sin \alpha_i}. \quad (18)$$

The main result of this section is that the vector field carried by the crease network is the appropriate field that measures the deformation of a rigid origami structure from the planar reference state. While it is known that the geometric degrees of freedom of an origami metamaterial can be formulated in terms

of the unit vectors tangent to the folds and the faces [26–29], the reduction to a single vector field parametrization of the total energy, including both the elastic energy of the crease network and the kinematic constraints, was lacking. Here we show that starting from the mechanical response of a single crease given by Eq. (2), the total elastic energy of an origami vertex, as given by Eq. (17), can be reduced to a functional of the vector field  $\vec{w}_i$  only.

Equation (17) allows us to develop a unified elastic formalism of origami metamaterials that can be applied to probe various mechanical properties. Although, we have considered the case of a single vertex of an arbitrary number of creases, the generalization to complex origami tessellations is straightforward (see Sec. VI). The equilibrium equations of a general origami vertex can be determined by minimizing Eq. (17) with respect to the vectors  $\vec{w}_i$  and the Lagrange multipliers  $\gamma_i$  and  $\delta_i$ . Nevertheless, to show the effectiveness of this elastic model we study in the following two special cases that allow for semianalytic resolution: the generalized waterbomb base and the Miura-Ori.

#### IV. GENERALIZED WATERBOMB BASE

We consider the origami vertex that consists in an alternation of  $n/2$  mountain and  $n/2$  valley folds of equal length  $L$ , separated by the same angle  $\alpha_i = \alpha = 2\pi/n$ , where  $n$  is the number of creases (see Fig. 5). The number of folds is even and for the rigid generalized waterbomb to exist, the condition  $n \geq 6$  must be fulfilled. The case  $n = 8$  corresponds to the usual waterbomb [30], a folding used as starting point of many origami constructions. We define a Cartesian coordinates system such that its origin is located at the vertex and the  $xy$  plane coincides with the reference planar state of the sheet before deformation. We consider configurations in which all valleys (respectively, mountains) have the same material parameters. Due to these symmetries, it is easy to show that the components of the crease vectors are given by:

$$\begin{aligned}\vec{w}_{2p} &= (\sin \theta_m \cos 2p\alpha, \sin \theta_m \sin 2p\alpha, \cos \theta_m), \\ \vec{w}_{2p+1} &= (\sin \theta_v \cos(2p+1)\alpha, \sin \theta_v \sin(2p+1)\alpha, \cos \theta_v),\end{aligned}\quad (19)$$

with  $p = 0, \dots, (n/2 - 1)$ . Here,  $\theta_m$  (respectively,  $\theta_v$ ) denotes the mountains (respectively, valleys) polar angles of the creases and we use the periodicity convention  $\vec{w}_0 \equiv \vec{w}_n$ . Also, the

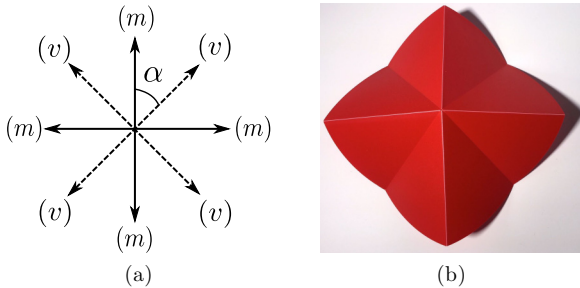


FIG. 5. The generalized waterbomb base. (a) The imprinted network. (b) Experimental realization of a three-dimensional equilibrium structure.

polar angles  $\theta_{m,v} \in [0, \pi]$  are chosen such that the reference plane of the sheet before deformation corresponds to  $\theta = \pi/2$ . Once these two angles are determined, the whole shape of the waterbomb is achieved.

For the generalized waterbomb base with  $n$ -folds, the elastic energy as given by Eq. (15) takes the following form:

$$\begin{aligned}E_W(\theta_m, \theta_v) &= \frac{\pi L}{\alpha \sin^2 \alpha} [\lambda_m (\cos^2 \alpha + \sin^2 \alpha \cos 2\theta_v) \\ &\quad + \lambda_v (\cos^2 \alpha + \sin^2 \alpha \cos 2\theta_m) \\ &\quad + \mu_m (\sin 2\alpha \sin^2 \theta_v \cos \theta_m - \sin \alpha \sin 2\theta_v \sin \theta_m) \\ &\quad + \mu_v (\sin 2\alpha \sin^2 \theta_m \cos \theta_v - \sin \alpha \sin 2\theta_m \sin \theta_v)],\end{aligned}\quad (20)$$

with:

$$\begin{aligned}\lambda_m &= -\kappa_m \cos \psi_m^0, & \mu_m &= -\kappa_m \sin \psi_m^0, \\ \lambda_v &= -\kappa_v \cos \psi_v^0, & \mu_v &= -\kappa_v \sin \psi_v^0,\end{aligned}\quad (21)$$

where  $(\kappa_m, \psi_m^0)$  and  $(\kappa_v, \psi_v^0)$  are, respectively, the stiffness and rest angle of the mountains and valleys. Recall that  $\psi_i$  is defined using the oriented angle from  $\vec{u}_i$  to  $\vec{v}_i$  which is equivalent to measuring crease angles on the same side of the folded sheet (Fig. 3). Therefore, we take the following convention for distinguishing mountains and valleys:  $\psi_m^0 \in [0, \pi]$  and  $\psi_v^0 \in [\pi, 2\pi]$ . In the following, we take  $\kappa_m = \kappa_v = \kappa$  and scale the elastic energy such that  $\kappa L = 1$ . The influence of the ratio  $\kappa_m/\kappa_v$  adds extra adjustability that is not crucial to the analysis [31].

Due to the symmetry of the waterbomb configuration, all the geometric constraints  $C_i$  in Eq. (8) amount to one relation between  $\theta_m$  and  $\theta_v$  given by:

$$C_W(\theta_m, \theta_v) = \cos \theta_m \cos \theta_v - \cos \alpha (1 - \sin \theta_m \sin \theta_v) = 0. \quad (22)$$

Because the valleys are always lower than the mountains, one has  $\theta_v \geq \theta_m$  and Eq. (22) yields:

$$\theta_v(\theta_m) = \begin{cases} \arccos\left(\frac{\cos \alpha \cos \theta_m}{1 + \sin \alpha \sin \theta_m}\right) & 0 \leq \theta_m \leq \frac{\pi}{2}, \\ \arccos\left(\frac{\cos \alpha \cos \theta_m}{1 - \sin \alpha \sin \theta_m}\right) & \frac{\pi}{2} < \theta_m \leq \pi - \alpha. \end{cases} \quad (23)$$

##### A. Equilibrium states of the waterbomb

We then minimize the elastic energy of the waterbomb, Eq. (20), subject to the geometric constraint (22) by introducing the energy functional:

$$E_W^* = E_W(\theta_m, \theta_v) - \gamma C_W(\theta_m, \theta_v), \quad (24)$$

where  $\gamma$  is a Lagrange multiplier. The extrema of Eq. (24) are found graphically by determining the points where the contour lines of the energy  $E(\theta_m, \theta_v)$  are tangent to the function  $\theta_v(\theta_m)$  given by Eq. (23). Figure 6 shows the existence of two equilibrium solutions: The system is always bistable. We label these solutions by  $(\pm)$ , the  $(+)$  state corresponding to the solution with  $\theta_m^+ \in [0, \frac{\pi}{2}]$  and the  $(-)$  state to the one with  $\theta_m^- \in [\frac{\pi}{2}, \pi]$  (see Fig. 7). These two equilibrium states can be experimentally obtained from one another through a snapping transition.

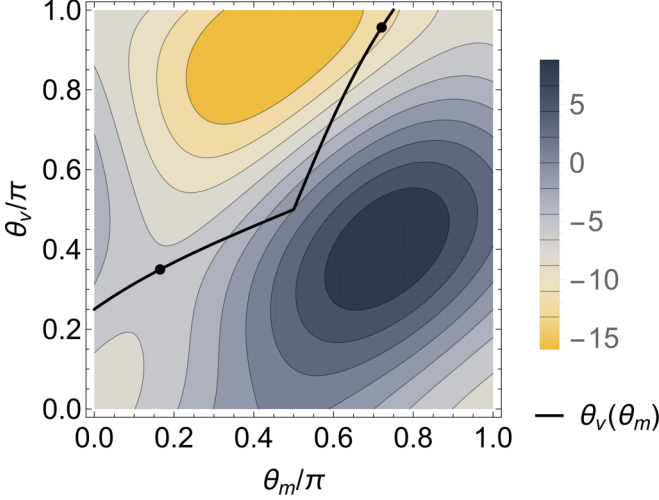


FIG. 6. Contour lines of the elastic energy, Eq. (20), of the waterbomb and the parametric curve of the geometric constraint, Eq. (23) (solid line). The two points on the curve correspond to the  $(\pm)$  equilibrium states. Here, the classical waterbomb ( $n = 8$ ) is displayed with creases elastic parameters  $\kappa_m = \kappa_v$ ,  $\psi_m^0 = \frac{\pi}{8}$ , and  $\psi_v^0 = 2\pi - \frac{\pi}{2}$ .

For  $\psi_v^0 = 2\pi - \psi_m^0$ , the bistability of this system is obvious. The elastic energy of this completely symmetric case given by Eq. (20) satisfies the symmetry property  $E_W(\theta_m, \theta_v) = E_W(\pi - \theta_v, \pi - \theta_m)$ , without imposing it *a priori*, and the geometric constraint (23) is always symmetric with respect to the line  $\theta_v = \pi - \theta_m$ :  $\mathcal{C}_W(\theta_m, \theta_v) = \mathcal{C}_W(\pi - \theta_v, \pi - \theta_m)$  (see Fig. 6). Therefore, in the complete symmetric case, one has  $\theta_v^\mp = \pi - \theta_m^\pm$ . That means that one solution is obtained from the other by a first rotation  $(\vec{e}_x, \pi)$  and a second rotation  $(\vec{e}_z, \alpha)$  to exchange mountains and valleys. As shown in Fig. 7, this symmetry property is suppressed when  $\psi_m^0 + \psi_v^0 \neq 2\pi$  and the two equilibrium solutions are not superimposable.

The minimization of the energy functional Eq. (24) can be easily carried out numerically. Figure 8 displays the variation of the resulting equilibrium angles  $\theta_m^\pm$  and  $\theta_v^\pm$  as function of the number of creases. These angles determine completely the equilibrium shapes of the waterbomb. On the other hand, we perform in Appendix a series expansion for a large number of creases that corresponds to small angles  $\alpha$  and find analytical expressions for  $\theta_m^\pm$  and  $\theta_v^\pm$  at linear order in  $\alpha$ . The results are shown in Fig. 8. It is worth pointing out that when  $n \rightarrow \infty$ ,

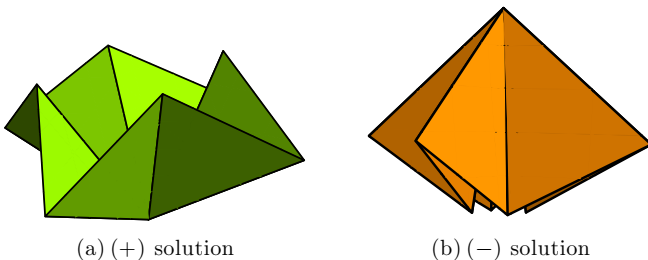


FIG. 7. The two equilibrium shapes of the waterbomb corresponding to the solutions of Fig. 6.

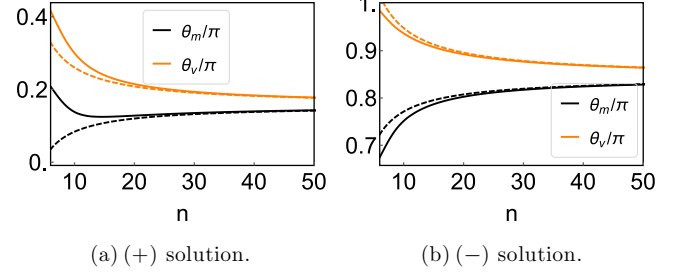


FIG. 8. Evolution of the two equilibrium solutions as a function of the number of creases for the same material parameters as in Fig. 6. Mountains angles are in black; valleys angles are in orange. The dashed curves correspond to the analytic results derived from the asymptotic expansions at first order in  $\alpha$  (see Appendix). Note that despite the fact that continuous curves are used, only those points corresponding to integer even  $n$  are physically relevant.

the equilibrium angles for mountains and valleys converge to the same limit  $\theta_\infty$  given by:

$$\theta_\infty = \begin{cases} \frac{\pi}{2} - \frac{\psi_v^0 - \psi_m^0}{4} & (+) \text{ solution,} \\ \frac{\pi}{2} + \frac{\psi_v^0 - \psi_m^0}{4} & (-) \text{ solution.} \end{cases} \quad (25)$$

Moreover, Fig. 8 shows that the equilibrium solutions for  $n \geq 16$  are well described by the analytical results of first-order expansions in  $\alpha$ , suggesting that the complete behavior for all  $n$  can be achieved by taking into account a few additional orders in the expansion.

Finally, we label  $\psi_m$  and  $\psi_v$  as the mountain and valley angles of the creases. Using Eqs (18) and (19), one can show that these angles are explicitly given by:

$$\cos \psi_m = \cos 2\theta_v \text{ and } 0 \leq \psi_m \leq \pi, \quad (26)$$

$$\cos \psi_v = \cos 2\theta_m \text{ and } \pi \leq \psi_v \leq 2\pi. \quad (27)$$

For a waterbomb structure, the behavior of the angles of the creases can then be directly extracted from their orientations.

By determining the equilibrium configurations of the generalized waterbomb, we have quantified the geometric frustration responsible for the deviation of the crease angles from their rest values and shown that the system is generically in a prestressed state even in the absence of external loading.

## B. Mechanical response of the waterbomb

The reference state of the waterbomb is set by the equilibrium solutions. To probe the mechanical response of the structure, a protocol for applying an external loading should be defined. The symmetry of the waterbomb configuration suggests using the same setup as the one for the developable cones [32]. Figure 9 shows a schematic of the experiment in which a vertical force  $F$  is applied at the vertex of the waterbomb base put on a cylinder of radius  $R < L$ . Depending on the solution considered, the waterbomb is in contact with the cylinder at either mountains or valleys creases. For the (+) solution [respectively, (-) solution], the applied force probes the response of the angle  $\theta_v$  (respectively,  $\theta_m$ ) from its equilibrium value.

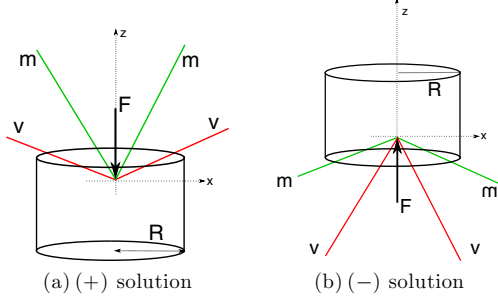


FIG. 9. Schematic of an experiment to study the mechanical response of a waterbomb depending on its equilibrium state.

Let us focus on the configuration of Fig. 9(a); the case of Fig. 9(b) follows the same steps. To calculate the stiffness of the structure, we note that the potential energy of a waterbomb deformed by a uniaxial force  $F^+$  in the  $z$  direction reads  $U = E_W - \int_{z_v^+}^z F^+(z) dz$ . The external force  $F^+(z)$  at equilibrium state is obtained by solving the equation  $\delta U / \delta \theta_v = 0$ :

$$F^+(z) = -\frac{\sin^2 \theta_v}{R} \frac{dE_W}{d\theta_v}. \quad (28)$$

We look for the linear response of the waterbomb near its equilibrium state:  $F^+(z) \simeq k^+(z - z_v^+)$ , where  $k^+$  is the stiffness of the vertex in the experimental situation of Fig. 9(a) and is given by

$$k_+ = \left. \frac{dF^+}{dz} \right|_{z=z_v^+} = \left. \frac{\sin^4 \theta_v^+}{R^2} \frac{d^2 E_W}{d\theta_v^2} \right|_{\theta_v=\theta_v^+}. \quad (29)$$

Figure 10 shows the variation of the normalized stiffnesses  $k_{\pm}$  with the number of creases. For both cases, we note that  $k_{\pm}$  is not monotonic in the number of creases. The stiffness of the generalized waterbomb is very large for  $n = 6$ , decreases with the number of creases for  $n > 6$ , and increases again linearly for large  $n$ , so there is an optimal waterbomb configuration for which the stiffness is minimum. For the cases depicted in Fig. 10, the minimum of  $k_+$  (respectively,  $k_-$ ) is reached for  $n_c^+ = 20$  (respectively,  $n_c^- = 22$ ). In the general case, the critical number of creases  $n_c^{\pm}$  depends on the material constants  $\kappa_m / \kappa_v$ ,  $\psi_m^0$ , and  $\psi_v^0$ .

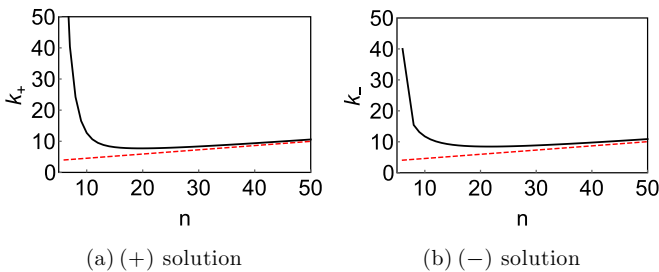


FIG. 10. The stiffnesses  $k_{\pm}$ , normalized by  $\kappa L / R^2$ , as function of the number of creases for the same material parameters as in Fig. 6. Asymptotic expansions are represented in red dashed curves. Integer even  $n$  are the only physically relevant points.

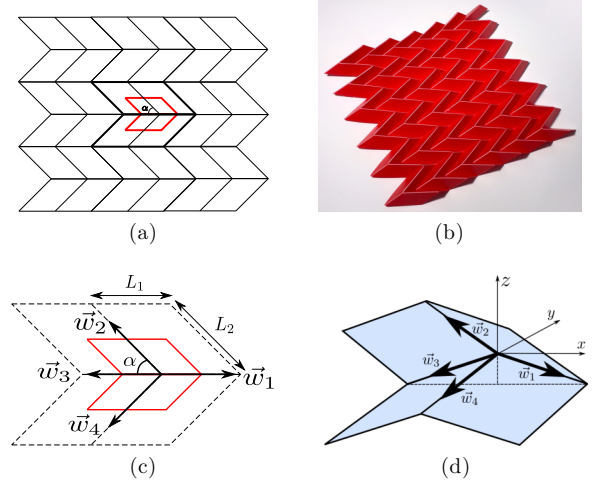


FIG. 11. Miura-Ori tessellation. (a) The imprinted network of creases. (b) Experimental realization of a three-dimensional equilibrium structure. (c) In the reference configuration, the unit cell is defined by the red polygonal contour. (d) The folded structure of the unit cell and its crease vectors deformation field  $\vec{w}_i$ .

## V. MIURA-ORI

The Miura-Ori (Fig. 11) is a periodic tessellation built from four equal parallelograms [16] characterized by two crease lengths ( $L_1, L_2$ ) and one plane angle  $\alpha \in [0, \pi/2]$  [Fig. 11(c)]. The vertex structure, with its three mountain and one valley folds [Fig. 11(d)], is similar to herringbone patterns that occur in leaves [10,11], fetal intestinal tissues [33], and biaxially compressed thin sheets supported on a substrate [34]. Thanks to its efficient packing-to-deployment ratio, it has been used to design solar sails for satellites [17] and incidentally folded maps [18]. Because the Miura-Ori includes basic elements of many origami structures, it has been proposed as a framework for origami metamaterials [3,4]. Although the approaches adopted in Refs. [3,4] are mainly geometrical, those works will serve as a guideline to this section in which we quantify the geometrical and mechanical properties of the Miura folding pattern.

In Fig. 11(c), we define the unit cell of the tessellation whose periphery does not include the crease network. This choice ensures that the elastic energy of all creases are taken into account and that all cells equally contribute, independently of their orientation with respect to the unit cell. In the Cartesian coordinates system of Fig. 11(d), the components of the crease unit vectors  $\vec{w}_i$  can be written as:

$$\begin{aligned} \vec{w}_1 &= (\sin \theta, 0, \cos \theta), & \vec{w}_3 &= (-\sin \theta, 0, \cos \theta), \\ \vec{w}_2 &= (\cos \phi, \sin \phi, 0), & \vec{w}_4 &= (\cos \phi, -\sin \phi, 0), \end{aligned} \quad (30)$$

where  $\theta$  denotes the angle of  $\vec{w}_1$  with respect to the  $z$  axis and  $\phi$  the angle of  $\vec{w}_2$  with respect to the  $x$  axis. The periodicity of the Miura tessellation imposes symmetry conditions to the folded configuration. Vectors  $\vec{w}_1$  and  $\vec{w}_3$  lie in the  $xz$  plane while  $\vec{w}_2$  and  $\vec{w}_4$  lie in the  $xy$  plane. Using Eq. (18), one finds

that the crease angles are given by:

$$\cos \psi_1 = \cos \psi_3 = 1 - 2 \left( \frac{\sin \phi}{\sin \alpha} \right)^2, \quad (31)$$

$$\cos \psi_2 = \cos \psi_4 = 2 \left( \frac{\cos \theta}{\sin \alpha} \right)^2 - 1. \quad (32)$$

The geometrical constraints  $C_i$  in Eq. (8) amount to one relation between  $\theta$  and  $\phi$  given by:

$$C_M(\theta, \phi) = \sin \theta \cos \phi + \cos \alpha = 0. \quad (33)$$

The geometry of the Miura-Ori is then entirely described by the four parameters  $(L_1, L_2, \alpha, \theta)$ ,  $\theta$  being the only degree of freedom of the system. Note that Eq. (33) reproduces in a simple and condensed expression the same geometrical conditions given in Refs. [3,4]. Last, taking  $0 < \alpha < \pi/2$  enforces the conditions  $\pi/2 \leq \theta \leq (\pi/2 + \alpha)$  and  $(\pi - \alpha) \leq \phi \leq \pi$ .

The symmetry properties of the Miura tessellation also impose conditions on the material constants  $\lambda_i$  and  $\mu_i$ : The stiffnesses and rest angles of the creases should satisfy

$$\begin{aligned} \kappa_1 = \kappa_3, \quad \psi_1^0 = 2\pi - \psi_3^0, \quad 0 < \psi_1^0 < \pi, \\ \kappa_2 = \kappa_4, \quad \psi_2^0 = \psi_4^0, \quad 0 < \psi_2^0 < \pi. \end{aligned} \quad (34)$$

Using Eq. (15), the elastic energy  $E_M$  of the unit cell is then given by:

$$\begin{aligned} \tilde{E}_M(\theta, \phi) &= \frac{\sin^2 \alpha}{L_1 \kappa_1} E_M(\theta, \phi) \\ &= -\cos \psi_1^0 \cos 2\phi - \beta \cos \psi_2^0 \cos 2\theta \\ &\quad - \sin \psi_1^0 \cos \theta \sin 2\phi + \beta \sin \psi_2^0 \sin 2\theta \sin \phi, \end{aligned} \quad (35)$$

where  $\tilde{E}_M$  is a dimensionless elastic energy that is independent of the static angle  $\alpha$ , and

$$\beta = \frac{\kappa_2 L_2}{\kappa_1 L_1}. \quad (36)$$

The elastic energy does not depend explicitly on  $L_2/L_1$  but rather on  $\beta$ , which embodies a mechanical-geometrical coupling. Finally, by applying adequate rotations of the unit cell, one can check that the energy of all cells in the Miura tessellation are also given by Eq. (35).

In the following, we present results for parameters values  $\beta = 1$  and  $\psi_1^0 = \psi_2^0 = \psi_0$ . The variation of these parameters adds extra adjustability that is not crucial to the analysis [31]. For this case, the geometric constraint (33) and the elastic energy (35) are invariant under the transformation  $(\theta, \phi, \psi_0) \rightarrow (3\pi/2 - \phi, 3\pi/2 - \theta, \pi - \psi_0)$ . This symmetry property allows us to explore the interval  $0 \leq \psi_0 \leq \pi/2$  and deduce the behavior for  $\pi/2 \leq \psi_0 \leq \pi$ .

#### A. Equilibrium states of the Miura-Ori

The equilibrium shape of the Miura-Ori is found by minimizing the elastic energy  $\tilde{E}_M$  given by Eq. (35) subject to the geometric constraint (33). This can be done by introducing the energy functional:

$$E_M^*(\theta, \phi, \gamma) = \tilde{E}_M(\theta, \phi) - \gamma C_M(\theta, \phi), \quad (37)$$

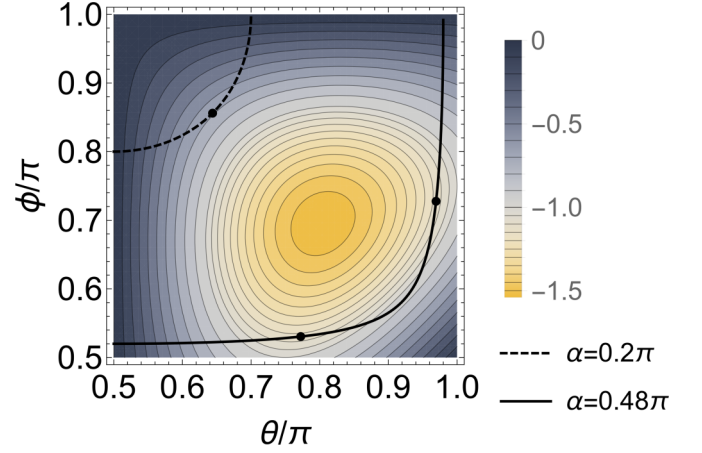


FIG. 12. Contour lines of the energy  $\tilde{E}_M(\theta, \phi)$  for  $\psi_0 = \pi/2$ . The two parametric curves correspond to the constraint  $C_M(\theta, \phi) = 0$  for two values of the plane angle  $\alpha$ . The points on the curves correspond to the different equilibrium states.

where  $\gamma$  is a Lagrange multiplier. The extrema of Eq. (37) are found graphically by determining the points where the contour lines of the energy  $\tilde{E}_M(\theta, \phi)$  are tangent to the solution  $\phi(\theta)$  of Eq. (33). The fact that  $\tilde{E}_M(\theta, \phi)$  is independent of the plane angle  $\alpha$  allows us to determine the equilibrium configurations for all values of  $\alpha$  using the same contour plot of  $\tilde{E}_M(\theta, \phi)$ .

Figure 12 shows that depending on the value of the plane angle, there is either a single equilibrium state or two metastable states. For a large range of values of  $\alpha$ , the system has one equilibrium configuration given by the minimum of  $\tilde{E}_M$  along the parametric curve  $C_M = 0$ . However for values of  $\alpha$  close to  $\pi/2$ , one finds two possible stable configurations separated by an unstable solution for which  $\tilde{E}_M$  is maximum along the parametric curve  $C_M = 0$ . This behavior is a generic signature of a phase transition controlled by the parameter  $\alpha$ . As will be shown below, the order of the transition depends on the rest angle of the creases  $\psi_0$ . Figure 13 shows the three dimensional shapes of the Miura folding corresponding to the equilibrium solutions of the cases depicted in Fig. 12. While the monostable state [Fig. 13(a)] reproduces a typical Miura-Ori configuration [3,4], the corresponding shape of the two metastable states differ considerably: The first configuration is closely packed [Fig. 13(b)] and the second one is widely deployed [Fig. 13(c)].

For a systematic study as function of the rest angle  $\psi_0$  and the static angle  $\alpha$ , we perform numerically the minimization of  $E_M^*$  given by Eq. (37) and determine the equilibrium angles  $\theta_s$  and  $\phi_s$ . The equilibrium crease angles  $\psi_{1s}$  and  $\psi_{2s}$  are then calculated *a posteriori* using Eqs. (31) and (32). Figures 14(a)–14(d) display the variation of  $\theta_s$  and  $\psi_{1s}$  as function of  $\alpha$  for two different rest angles  $\psi_0$ . In addition to the main continuous branch of solutions, a second equilibrium state develops when the static angle approaches  $\pi/2$ . The transition from a monostable to two metastable states is generically of first order. However, the case of a rest angle  $\psi_0 = \pi/2$  is peculiar: The two branches merge at  $\alpha_c \simeq 0.446$ , undergoing a second-order transition characterized by a pitchfork bifurcation. Moreover, one notes that for  $\psi_0 < \pi/2$  (respectively,  $\psi_0 > \pi/2$ ) the continuous branch of solutions

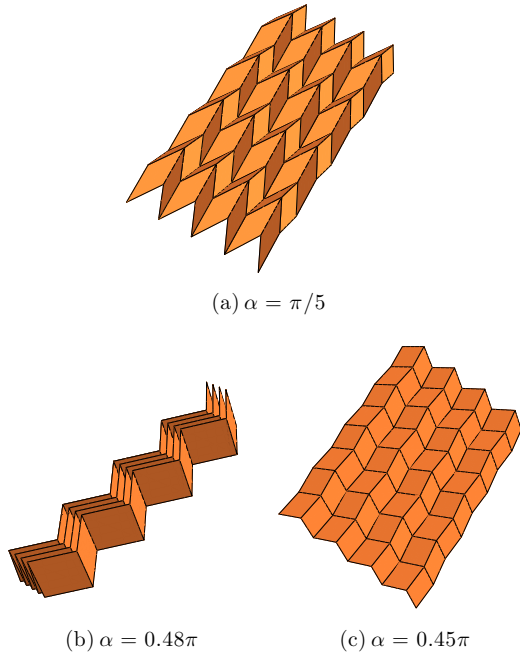


FIG. 13. Equilibrium configurations of the Miura-Ori for the same parameters as in Fig. 12 and  $L_1 = L_2$ . (a) For  $\alpha = \pi/5$ , there is one equilibrium state. [(b) and (c)] For  $\alpha = 0.48\pi$ , the system has two metastable states with one configuration that is approximately flat-folded and the second one that is widely deployed.

$\theta_s(\alpha)$  correspond to the folded (respectively, deployed) state, while the second equilibrium solution that occurs for  $\alpha > \alpha_c(\psi_0)$  corresponds to the deployed (respectively, folded) state of the Miura-ori.

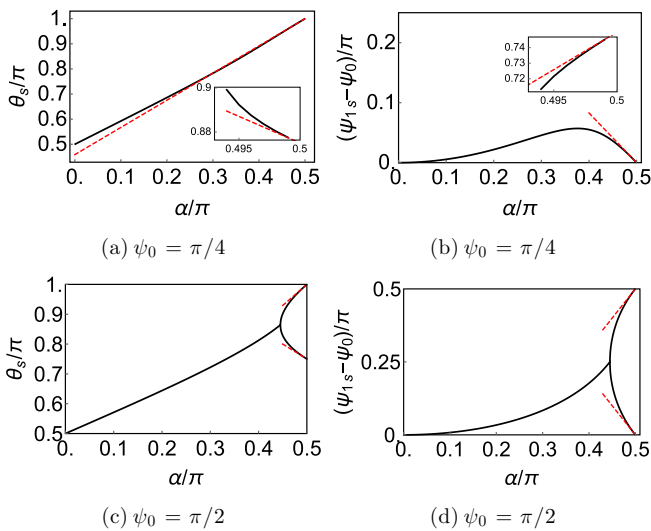


FIG. 14. Evolution of the equilibrium angles  $\theta_s$  [(a) and (c)] and their corresponding crease angles  $\psi_{1s}$  [(b) and (d)] as function of the static angle  $\alpha$  for two values of  $\psi_0$ . Red dashed curves correspond to asymptotic analytical solutions for  $\alpha \rightarrow \pi/2$  (see Appendix). Note that insets in (a) and (b) correspond to the second equilibrium state that exists for  $\alpha > \alpha_c(\psi_0)$ .

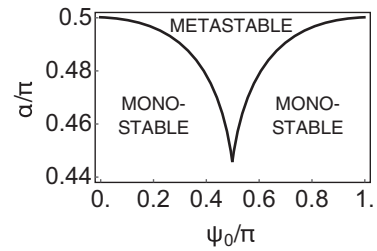
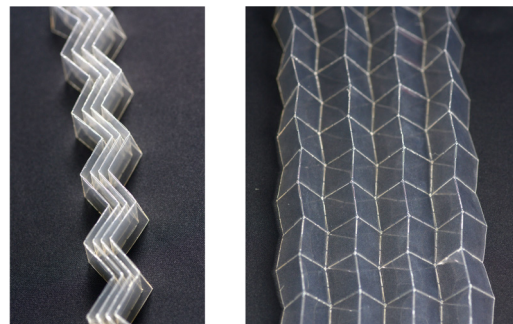


FIG. 15. Phase diagram  $(\alpha, \psi_0)$  of the different equilibrium configurations of Miura folding for material parameters satisfying  $\psi_1^0 = \psi_2^0 = \psi_0$  and  $\beta = 1$ .

The phase diagram of the Miura-Ori equilibrium states is determined by computing the threshold  $\alpha_c(\psi_0)$  above which the system becomes bistable. Figure 15 shows that the domain of existence of bistable solutions is always narrow and corresponds to quasirectangular building-block parallelograms. The phase diagram provides a quantitative tool for designing one monostable or bistable structures and rationalizes the observations that optimal Miura-Ori reversible deployable structures, such as solar sails or folded maps, should be designed with a plane angle  $\alpha$  close to  $\pi/2$  [17,18]. An experimental realization of a bistable state and images of a Miura-Ori folded map are shown in Fig. 16.

Finally, to study the relative stability of the folded and deployed states, the energy landscape  $\tilde{E}_M$  along the curve



(a) Folded state (b) Deployed state



(c) Folded state (d) Deployed state

FIG. 16. [(a) and (b)] Experimental realization of a bistable equilibrium configuration of Miura-Ori with a plane angle  $\alpha = 85^\circ$ . The material used is a printable transparency film. [(c) and (d)] The bistable equilibrium states of a Miura-Ori folded map with a plane angle  $\alpha \approx 88^\circ$  (from Miura-ori Lab).

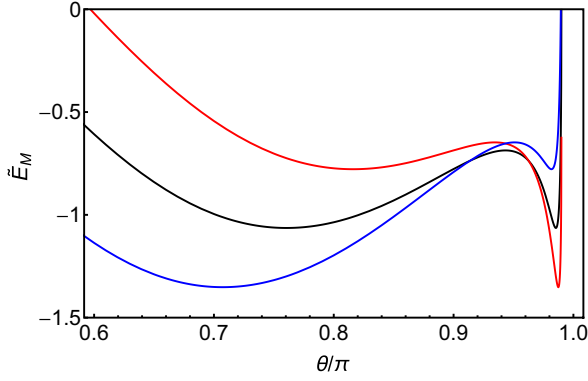


FIG. 17. The energy landscape of a Miura-ori  $\tilde{E}_M(\theta, \phi(\theta))$  with  $\phi(\theta)$  given by the geometric constraint (33). The different curves correspond to  $\alpha = 0.49\pi$  and to rest angles  $\psi_0 = 0.4\pi$  (red),  $\pi/2$  (black), and  $0.6\pi$  (blue).

satisfying the geometric constraint (33) is computed for values of static and rest angles allowing for two equilibrium states. Figure 17 shows that for  $\psi_0 < \pi/2$  (respectively,  $\psi_0 > \pi/2$ ), the global energy minimum corresponds to the folded (respectively, deployed) configuration. For  $\psi_0 \neq \pi/2$ , the second equilibrium state that appears for  $\alpha > \alpha_c(\psi_0)$  is a local minimum. For  $\psi_0 = \pi/2$ , the two equilibrium states are degenerate and the stability of the folded and deployed configurations is thus maximized. Creases in real origami structures exhibit viscous response and relaxation [21] and could smear out the secondary minima when deployment or folding is attempted at finite speed due to transient stresses. In such situations, the corresponding metastable configurations would appear unstable and difficult to reach. However, the intrinsic bistability of Miura-Ori can be enhanced by fine-tuning the crease stiffnesses and rest angles.

### B. Mechanical response of the Miura-Ori

To study the mechanical response of the Miura-Ori, one should consider the equilibrium solutions as reference states and define a protocol for applying an external loading. Here we choose to apply equally on each vertex of the tessellation a force  $F_z$  along the  $z$  axis [see Fig. 11(d)]. The external force  $F_z(z)$  at equilibrium state is given by:

$$F_z(z) = \frac{dE_M}{dz} = \frac{\kappa_1}{\sin^2 \alpha \sin \theta} \frac{d\tilde{E}_M}{d\theta}, \quad (38)$$

where  $dz = L_1 \sin \theta d\theta$ . We look for the linear response of the system near its equilibrium state:  $F_z(z) \simeq k_z(z - z_s)$ , where  $k_z$  is the stiffness of the Miura fold in the  $z$  direction given by:

$$k_z = \frac{\kappa_1}{L_1 \sin^2 \alpha \sin^2 \theta_s} \left. \frac{d^2 \tilde{E}_M}{d^2 \theta} \right|_{\theta=\theta_s}. \quad (39)$$

Note that the stiffnesses  $k_x$  and  $k_y$  can be determined following similar probing procedures [4]. Figure 18(a) shows the stiffness of the different equilibrium configurations as a function of the static angle  $\alpha$ . For the main branch,  $k_z$  is not monotonic and there exists an optimal  $\alpha$  for which the stiffness is minimal. In the bistable phase, we find that the stiffness of the deployed state is three orders of magnitude

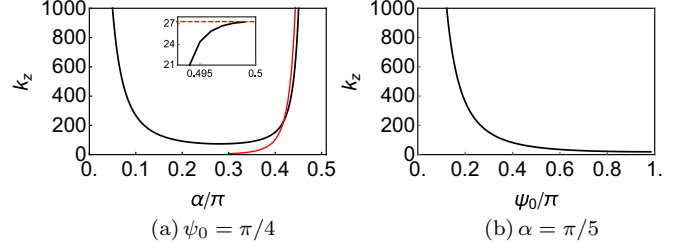


FIG. 18. The stiffness  $k_z$ , normalized by  $\kappa_1/L_1$  for two parameter cases: (a)  $k_z(\alpha, \psi_0 = \pi/4, \beta = 1)$ . (b)  $k_z(\alpha = \pi/5, \psi_0, \beta = 1)$ . In (a) the Inset corresponds to the stiffness of the second stable branch and the red dashed curves to asymptotic expansions for  $\alpha \rightarrow \pi/2$ .

softer than the stiffness of its corresponding folded state. This property is indeed suitable for deployable structures. In addition, Fig. 18(b) shows that for fixed static angle  $\alpha$  in the monostable phase, the stiffness  $k_z$  is a monotonically decreasing function of  $\psi_0$ .

We also study the coupling of deformations of the equilibrium solutions. Following Refs. [3,4], we define the linearized in-plane Poisson's ratio  $\nu$  as the ratio between the transverse strain (in the  $y$  direction) and the axial strain (in the  $x$  direction) of the Miura fold. This yields:

$$\nu = 1 - \frac{1}{\sin^2 \alpha \sin^2(\psi_1/2)}. \quad (40)$$

Figure 19 shows the expected result that  $\nu$  is always negative [3,4], so the Miura-Ori is an auxetic material with respect to deformations in the  $xy$  plane. The general behavior also qualitatively follows the results of Refs. [3,4]. In addition, for  $\alpha \simeq \pi/2$ , we show that the Poisson's ratio of the deployed solution scales as  $(\pi/2 - \alpha)^2$  while it tends to a finite constant for the folded state [see Appendix and Fig. 19(a)].

## VI. DISCUSSION

We have developed an elastic theory of rigid origami structures in which deformations are mediated by a crease network that acts as a series of hinges connecting infinitely rigid panels. Starting from a vectorial description of a single crease, we introduce a covariant elastic energy that naturally embodies a nonlinear behavior without adding additional material constants besides crease stiffness and rest angle. For a single vertex with arbitrary number of creases coming from it, we performed simple geometric manipulations expressing rigid-face conditions to write both the elastic energy of the vertex and the geometric constraints in terms of the crease

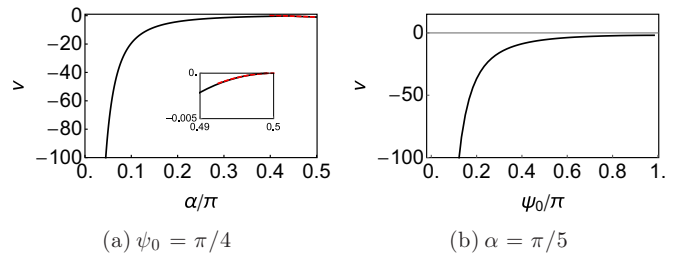


FIG. 19. Poisson's ratio  $\nu$  for the same two parameter cases as in Fig. 18.

vectors only. This result allows us to define the vector field carried by the crease network as the appropriate field for quantifying elastic deformations of origami structures with respect to the planar reference configuration.

We then applied this model to the generalized waterbomb and to Miura's periodic tessellation. These two cases were chosen because of the single degree of freedom they exhibit, making a systematic analytical analysis possible. For the waterbomb, we show a generic bistability of this system for any number of creases. For the Miura folding, we uncover a phase transition from monostable to bistable states that explains the efficient deployability of this structure for a given range of geometrical and mechanical parameters. Our study provides a quantitative and mechanical basis for the property of large volume ratio between the deployed and folded states of Miura-Ori designs used for map folding and solar sails. Moreover, we show that geometric frustration forces us to define the equilibrium configuration as a reference state for the study of mechanical response of folded structures. The analysis of the waterbomb and Miura-Ori cases demonstrates the power of using the vectors supported by the crease network as a parametrization of the elastic deformation.

One could argue that our results, especially the bistable behavior of Miura-ori, depend on the specific modeling of the crease energy. Effectively, Eqs. (2) and (4) can be regarded as the first-order terms in a Fourier expansion of the experimentally established quadratic form (5) [22]. However, a careful inspection of Fig. 15 shows that the extent of the bistable region in the  $(\psi_0, \alpha)$  parameter space is maximum for  $\psi_0 = \pi/2$ , a rest angle for which the difference between the covariant (2) and quadratic (5) forms of the crease energy is minimum. Our results show indeed that Miura-Ori fourfold vertices share the same behavior as general four-degree vertices which are known to be generically multibranching and at least bistable [5].

Until now, we considered rigid origami tessellations that can be reduced to a unit cell described by a single  $n$ -degree vertex. However, our approach can be extended to arbitrary networks for which the deformation of the crease vector field is a natural description. More precisely, consider a general origami tessellation built on an imprinted two-dimensional undirected planar graph  $G$  of size (number of vertices)  $N_v$ . The associated network is defined by an adjacency matrix  $a_{ij}$  [35], the degree  $k_i \geq 4$  of each vertex [5], and the number of faces  $N_f$ . For each edge  $(i, j)$  connecting two adjacent vertices, we define the symmetric matrix elements  $(L_{ij}, \lambda_{ij}, \mu_{ij})$  as the length and material constants of the corresponding crease. The angles  $\alpha_{ij}^\pm$  between the edge  $(i, j)$  and its two adjacent edges at the vertex  $i$  are also prescribed. Finally, we introduce the vector deformation field of the network  $\vec{w}_{ij}$  running out from vertex  $i$  to its adjacent one  $j$ . This definition of the vector deformation field allows us to decouple the elastic energies

of the vertices  $i$  and  $j$ . The condition  $\vec{w}_{ij} = -\vec{w}_{ji}$  should be imposed as a constraint in the energy functional. However, this condition is in general not sufficient to reconstruct the crease network. One must also impose  $N_f$  additional constraints that ensure a closed path for any oriented loop along the crease network. These conditions, noted for simplicity  $\mathcal{F}_i = 0$ , are satisfied when the sum of the adjacent fold vectors  $L_{ij}\vec{w}_{ij}$  around each face vanishes. The Lagrangian  $E_G^*$  of the crease network in its folded state can then be written as:

$$E_G^* = \frac{1}{2} \sum_{i=1}^{N_v} E_i^* (\{a_{ij}\vec{w}_{ij}; j = 1, \dots, N\}) + \sum_{i=1}^{N_v} \sum_{j=1}^{N_v} \rho_{ij} a_{ij} |\vec{w}_{ij} + \vec{w}_{ji}|^2 + \sum_{i=1}^{N_f} \Gamma_i \mathcal{F}_i, \quad (41)$$

where the elastic energy  $E_i^*$  of each vertex is given by Eq. (17),  $\rho_{ij}$  and  $\Gamma_i$  are Lagrange multipliers, and the coefficient  $1/2$  takes into account the double counting of each edge in the sum.

Therefore, the elastic energy of rigid origami can be formally written for any arbitrary crease network. This makes this approach relevant for studying complex structures, be it periodic tessellations built upon unit cells of more than one vertex such as Resch patterns [23], or disordered networks such as crumpled paper [24]. Moreover, Eq. (41) is suitable for performing local mechanical perturbations that allow for studying vibrational modes and elastic interactions with and between topological defects [29].

Finally, this formalism can also be extended to the situation in which the condition of infinitely rigid faces is relaxed. Indeed, when elastic deformations of the faces are taken into account, the shape of the crease is generally curved and must be determined as the solution of a minimization problem [25,36]. For the case of a single curved crease joining two flexible panels, the total energy of this structure is the sum of elastic energies of the faces, induced by bending deformations, and the crease elastic energy. The energy  $\mathcal{E}$  in Eq. (2) is local along the crease and thus can be generalized to creases with arbitrary shapes. Figure 1 shows that the vector fields  $(\vec{w}, \vec{u})$  and  $(\vec{w}, \vec{v})$  are the local tangent and normal unit vectors of the Frenet-Serret frames of each panel along the crease. Therefore, the covariant formulation given by Eq. (2) allows us to express the total elastic energy in terms of the same deformation field and thus to perform energy minimization properly.

## ACKNOWLEDGMENTS

We thank S. Waitukaitis for discussions on origami modeling. This research was supported by the ANR-14-CE07-0031 METAMAT.

## APPENDIX: ASYMPTOTIC EXPANSIONS

### 1. Generalised waterbomb

In the following, we look for equilibrium solutions of the waterbomb structure in the limit of large number of creases ( $\alpha \ll 1$ ). Let us write the angles  $\theta_m$  and  $\theta_v$  as:

$$\theta_m = \theta_\infty + f_1 \alpha + O(\alpha^2), \quad (A1)$$

$$\theta_v = \theta_\infty + g_1 \alpha + O(\alpha^2). \quad (\text{A2})$$

Using these expansions, the perturbation of the geometric constraint Eq. (22) yields

$$\frac{1}{2}(\cos^2 \theta_\infty - (f_1 - g_1)^2) \alpha^2 + O(\alpha^3) = 0. \quad (\text{A3})$$

This gives:

$$f_1 = g_1 \pm \cos \theta_\infty. \quad (\text{A4})$$

These two cases correspond to the ( $\pm$ ) solutions. Here we detail only the (+) solution and give the final results of the (−) solution.

For the (+) solution, one has  $\theta_\infty \in [0, \frac{\pi}{2}]$  and the condition  $\theta_m < \theta_v$  gives:

$$f_1 = g_1 - \cos \theta_\infty. \quad (\text{A5})$$

We are then left with two unknowns,  $\theta_\infty$  and  $g_1$ . For the case  $\kappa_m = \kappa_v$ , the series expansion of the elastic energy Eq. (20) yields:

$$\begin{aligned} E_W(\theta_\infty, g_1) = & -(\cos \psi_m^0 + \cos \psi_v^0) \alpha + 2 \sin \theta_\infty [\sin(\theta_\infty - \psi_m^0) + \sin(\theta_\infty + \psi_v^0)] \alpha^2 \\ & + 2[g_1 \sin(2\theta_\infty - \psi_m^0) + (g_1 - \cos \theta_\infty) \sin(2\theta_\infty + \psi_v^0)] \alpha^3 + O(\alpha^4). \end{aligned} \quad (\text{A6})$$

Energy minimization is carried out by differentiating with respect to  $\theta_\infty$  and  $g_1$ . This gives:

$$\frac{\partial E_W}{\partial g_1} = 0 = 2\alpha^3 [\sin(2\theta_\infty - \psi_m^0) + \sin(2\theta_\infty + \psi_v^0)] + O(\alpha^4), \quad (\text{A7})$$

$$\begin{aligned} \frac{\partial E_W}{\partial \theta_\infty} = 0 = & 2[\sin(2\theta_\infty - \psi_m^0) + \sin(2\theta_\infty + \psi_v^0)] \alpha^2 + 2[2g_1 \cos(2\theta_\infty - \psi_m^0) + 2(g_1 - \cos \theta_\infty) \cos(2\theta_\infty + \psi_v^0) \\ & + \sin \theta_\infty \sin(2\theta_\infty + \psi_v^0)] \alpha^3 + O(\alpha^4). \end{aligned} \quad (\text{A8})$$

Then, at this order in the perturbation one is left with two equations:

$$\sin(2\theta_\infty - \psi_m^0) + \sin(2\theta_\infty + \psi_v^0) = 0, \quad (\text{A9})$$

$$2g_1 \cos(2\theta_\infty - \psi_m^0) + 2(g_1 - \cos \theta_\infty) \cos(2\theta_\infty + \psi_v^0) + \sin \theta_\infty \sin(2\theta_\infty + \psi_v^0) = 0. \quad (\text{A10})$$

Using the definitions  $\psi_m^0 \in [0, \pi]$  and  $\psi_v^0 \in [\pi, 2\pi]$ , one can show that the solutions for  $\theta_\infty \in [0, \frac{\pi}{2}]$  and  $g_1$  are given by:

$$\theta_\infty = \frac{\pi}{2} + \frac{\psi_m^0 - \psi_v^0}{4}, \quad (\text{A11})$$

$$g_1^+ = \frac{1}{8 \cos \frac{\psi_m^0 + \psi_v^0}{2}} \left( \sin \frac{\psi_m^0 + 3\psi_v^0}{4} - 3 \sin \frac{3\psi_m^0 + \psi_v^0}{4} \right). \quad (\text{A12})$$

Therefore the asymptotic expansions at first order in  $\alpha$  of the equilibrium angles follow:

$$\theta_m^+ = \frac{\pi}{2} + \frac{\psi_m^0 - \psi_v^0}{4} + \frac{1}{8 \cos \frac{\psi_m^0 + \psi_v^0}{2}} \left( \sin \frac{3\psi_m^0 + \psi_v^0}{4} - 3 \sin \frac{\psi_m^0 + 3\psi_v^0}{4} \right) \alpha + O(\alpha^2), \quad (\text{A13})$$

$$\theta_v^+ = \frac{\pi}{2} + \frac{\psi_m^0 - \psi_v^0}{4} + \frac{1}{8 \cos \frac{\psi_m^0 + \psi_v^0}{2}} \left( \sin \frac{\psi_m^0 + 3\psi_v^0}{4} - 3 \sin \frac{3\psi_m^0 + \psi_v^0}{4} \right) \alpha + O(\alpha^2). \quad (\text{A14})$$

Using these results, one can perform the series expansion of the stiffness. Equation (29) can be rewritten as:

$$k_+ = \sin^4 \theta_v \left[ \frac{\partial^2 E_W}{\partial \theta^2} + 2 \frac{d\theta_m}{d\theta_v} \frac{\partial E_W}{\partial \theta_m \partial \theta_v} + \left( \frac{d\theta_m}{d\theta_v} \right)^2 \frac{\partial^2 E_W}{\partial \theta_m^2} \right] \Big|_{\theta_v = \theta_v^+}, \quad (\text{A15})$$

where  $k_+$  is scaled by  $\kappa L/R^2$ . After straightforward computations, one finds

$$\begin{aligned} k_+ = & -\cos^4 \frac{\psi_m^0 - \psi_v^0}{4} \cos \frac{\psi_m^0 + \psi_v^0}{2} [7 + \cos(\psi_m^0 - \psi_v^0)] \frac{\pi}{\alpha} + \frac{\pi}{32} \cos^3 \frac{\psi_m^0 - \psi_v^0}{4} \\ & \times \left[ 55 \cos \psi_m^0 + 65 \cos \psi_v^0 - 3 \cos(\psi_m^0 - 2\psi_v^0) + 11 \cos(2\psi_m^0 - \psi_v^0) - 48[7 + \cos(\psi_m^0 - \psi_v^0)] \cos \frac{\psi_m^0 + \psi_v^0}{2} \right] + O(\alpha). \end{aligned} \quad (\text{A16})$$

By carrying out similar computations for the (−) solution, one obtains:

$$\theta_m^- = \frac{\pi}{2} + \frac{\psi_v^0 - \psi_m^0}{4} + \frac{1}{8 \cos \frac{\psi_m^0 + \psi_v^0}{2}} \left( \sin \frac{3\psi_m^0 + \psi_v^0}{4} - 3 \sin \frac{\psi_m^0 + 3\psi_v^0}{4} \right) \alpha + O(\alpha^2), \quad (\text{A17})$$

$$\theta_v^- = \frac{\pi}{2} + \frac{\psi_v^0 - \psi_m^0}{4} + \frac{1}{8 \cos \frac{\psi_m^0 + \psi_v^0}{2}} \left( \sin \frac{\psi_m^0 + 3\psi_v^0}{4} - 3 \sin \frac{3\psi_m^0 + \psi_v^0}{4} \right) \alpha + O(\alpha^2), \quad (\text{A18})$$

and

$$k_- = -\cos^4 \left( \frac{\psi_m^0 - \psi_v^0}{4} \right) \cos \frac{\psi_m^0 + \psi_v^0}{2} [7 + \cos(\psi_m^0 - \psi_v^0)] \frac{\pi}{\alpha} + \frac{\pi}{32} \cos^3 \frac{\psi_m^0 - \psi_v^0}{4} \left\{ 55 \cos \psi_v^0 + 65 \cos \psi_m^0 \right. \\ \left. - 3 \cos(\psi_v^0 - 2\psi_m^0) + 11 \cos(2\psi_v^0 - \psi_m^0) - 48[7 + \cos(\psi_m^0 - \psi_v^0)] \cos \frac{\psi_m^0 + \psi_v^0}{2} \right\} + O(\alpha). \quad (\text{A19})$$

## 2. Miura-Ori

In the following, we look for equilibrium solutions of the Miura-Ori tessellation when the static angle  $\alpha$  is close to  $\pi/2$ . We solve this problem in the general case for any given material parameters  $\beta$ ,  $\psi_1^0$ , and  $\psi_2^0$ . Define  $\alpha = \pi/2 - \epsilon$ , with  $0 \leq \epsilon \ll 1$  and:

$$\theta = \theta_0 + f_1 \epsilon + O(\epsilon^2), \quad (\text{A20})$$

$$\phi = \phi_0 + g_1 \epsilon + O(\epsilon^2). \quad (\text{A21})$$

The series expansion of Eq. (33) to first order in  $\epsilon$  yields:

$$\mathcal{C}_M(\theta, \phi) = \sin \theta_0 \cos \phi_0 + (1 + f_1 \cos \theta_0 \cos \phi_0 - g_1 \sin \theta_0 \sin \phi_0) \epsilon + O(\epsilon^2). \quad (\text{A22})$$

The geometrical constraint  $\mathcal{C}_M = 0$  gives:

$$\sin \theta_0 \cos \phi_0 = 0, \quad (\text{A23})$$

$$g_1 \sin \theta_0 \sin \phi_0 - f_1 \cos \theta_0 \cos \phi_0 = 1. \quad (\text{A24})$$

Equation (A23) admits two solutions: either  $\theta_0 = \pi$  or  $\phi_0 = \pi/2$ . Here we detail only the case  $\theta_0 = \pi$  and give the final results for the case  $\phi_0 = \pi/2$ .

Using the solution  $\theta_0 = \pi$ , Eq. (A24) reduces to:

$$f_1 = \frac{1}{\cos \phi_0}. \quad (\text{A25})$$

We are then left with two unknowns,  $\phi_0$  and  $g_1$ . The series expansion of the elastic energy as given by Eq. (35) gives:

$$\tilde{E}_M(\phi_0, g_1) = -[\cos(2\phi_0 + \psi_1^0) + \beta \sin \psi_2^0] + 2[g_1 \sin(2\phi_0 + \psi_1^0) + \beta \sin \psi_2^0 \tan \phi_0] \epsilon + O(\epsilon^2). \quad (\text{A26})$$

Energy minimization is carried out by differentiating with respect to  $\phi_0$  and  $g_1$ . This gives:

$$\frac{\partial \tilde{E}_M}{\partial \phi_0} = 0 = 2 \sin(2\phi_0 + \psi_1^0) + 2 \left[ 2g_1 \cos(2\phi_0 + \psi_1^0) + \beta \frac{\sin \psi_2^0}{\cos^2 \phi_0} \right] \epsilon + O(\epsilon^2), \quad (\text{A27})$$

$$\frac{\partial \tilde{E}_M}{\partial g_1} = 0 = 2 \sin(2\phi_0 + \psi_1^0) \epsilon + O(\epsilon^2). \quad (\text{A28})$$

Then, at this order in the perturbation, one is left with two equations:

$$\sin(2\phi_0 + \psi_1^0) = 0, \quad (\text{A29})$$

$$2g_1 \cos(2\phi_0 + \psi_1^0) + \beta \frac{\sin \psi_2^0}{\cos^2 \phi_0} = 0. \quad (\text{A30})$$

Using the definitions  $\phi_0 \in [\frac{\pi}{2}, \pi]$  and  $\psi_1 \in [0, \pi]$ , one can show that the solutions for  $\phi_0$  and  $g_1$  are given by:

$$\phi_0 = \pi - \frac{\psi_1^0}{2}, \quad (\text{A31})$$

$$g_1 = -\frac{\beta \sin \psi_2^0}{\cos \psi_1^0 + 1}. \quad (\text{A32})$$

Therefore the asymptotic expansions to first order in  $\epsilon$  of the equilibrium angles follow as:

$$\theta_s = \pi - \frac{1}{\cos(\psi_1^0/2)} \epsilon + O(\epsilon^2), \quad (\text{A33})$$

$$\phi_s = \pi - \frac{\psi_1^0}{2} - \frac{\beta \sin \psi_2^0}{\cos \psi_1^0 + 1} \epsilon + O(\epsilon^2). \quad (\text{A34})$$

Using these results, one can derive from Eqs. (31) and (32) the series expansion of the equilibrium crease angles  $\psi_{1s}$  and  $\psi_{2s}$ :

$$\psi_{1s} = \psi_1^0 + \frac{2\beta \sin \psi_2^0}{\cos \psi_1^0 + 1} \epsilon + O(\epsilon^2), \quad (\text{A35})$$

$$\psi_{2s} = 2\epsilon \tan \frac{\psi_1^0}{2} + O(\epsilon^2), \quad (\text{A36})$$

and the series expansion of the Poisson's ratio as given by Eq. (40) reads

$$\nu = -\frac{1}{\tan^2(\psi_1^0/2)} + \frac{8\beta \sin \psi_2^0}{2 \sin \psi_1^0 - \sin 2\psi_1^0} \epsilon + O(\epsilon^2). \quad (\text{A37})$$

Finally, the series expansion of Eq. (39) that defines the stiffness  $k_z$  yields

$$k_z = \frac{(1 + \cos \psi_1^0)^3}{4(1 - \cos \psi_1^0)} \left[ 1 + \frac{3}{\sqrt{2}} + 3(3 - \sqrt{2}) \cos \psi_1^0 - \frac{3}{\sqrt{2}}(\sqrt{2} - 1) \cos 2\psi_1^0 \right] \epsilon^{-4} + O(\epsilon^{-3}), \quad (\text{A38})$$

where  $k_z$  is scaled by  $\kappa_1/L_1$ .

By carrying out similar computations for the solution  $\phi_0 = \pi/2$ , one obtains:

$$\begin{aligned} \theta_s &= \pi - \frac{\psi_2^0}{2} + \frac{\sin \psi_1^0}{\beta(1 - \cos \psi_2^0)} \epsilon + O(\epsilon^2), & \phi_s &= \frac{\pi}{2} + \frac{1}{\sin(\psi_2^0/2)} \epsilon + O(\epsilon^2), \\ \psi_{1s} &= \pi - \frac{2}{\tan(\psi_1^0/2)} \epsilon + O(\epsilon^2), & \psi_{2s} &= \psi_2^0 - \frac{2 \sin \psi_1^0}{\beta(1 - \cos \psi_2^0)} \epsilon + O(\epsilon^2), \\ \nu &= \frac{-2}{1 - \cos \psi_2^0} \epsilon^2 + O(\epsilon^4), & k_z &= \frac{8\beta}{1 - \cos \psi_2^0} + O(\epsilon^2). \end{aligned} \quad (\text{A39})$$

Note that the two equilibrium solutions exist for all values of  $0 \leq \psi_1^0 < \pi$  and  $0 < \psi_2^0 \leq \pi$ . For  $\psi_1^0 = \pi$  (respectively,  $\psi_2^0 = 0$ ), the only solution that persists is the one that corresponds to the branch  $\phi_0 = \pi/2$  (respectively,  $\theta_0 = \pi$ ).

- 
- [1] E. D. Demaine, *Folding and Unfolding*, Ph.D. Thesis, University of Waterloo, 2001.
- [2] E. D. Demaine and J. O'Rourke, *Geometric Folding Algorithms: Linkages, Origami, Polyhedra* (Cambridge University Press, Cambridge, 2007).
- [3] M. Schenk and S. D. Guest, *Proc. Natl. Acad. Sci. USA* **110**, 3276 (2013).
- [4] Z. Y. Wei, Z. V. Guo, L. Dudte, H. Y. Liang, and L. Mahadevan, *Phys. Rev. Lett.* **110**, 215501 (2013).
- [5] S. Waitukaitis, R. Menaut, Bryan Gin-gie Chen, and M. van Hecke, *Phys. Rev. Lett.* **114**, 055503 (2015).
- [6] J. L. Silverberg, J.-H. Na, A. A. Evans, B. Liu, T. C. Hull, C. D. Santangelo, R. J. Lang, R. C. Hayward, and I. Cohen, *Nat. Mater.* **14**, 389 (2015).
- [7] F. Lechenault and M. Adda-Bedia, *Phys. Rev. Lett.* **115**, 235501 (2015).
- [8] J. L. Silverberg, A. A. Evans, L. McLeod, R. C. Hayward, T. Hull, C. D. Santangelo, and I. Cohen, *Science* **345**, 647 (2014).
- [9] F. Haas and R. J. Wootton, *Proc. R. Soc. London B* **263**, 1651 (1996).
- [10] H. Kobayashi, B. Kresling, and J. F. V. Vincent, *Proc. R. Soc. Lond. B* **265**, 147 (1998).
- [11] E. Couturier, S. Courrech du Pont, and S. Douady, *PloS One* **4**, e7968 (2009).
- [12] H. W. Holdaway, *Text. Res. J.* **30**, 296 (1960).
- [13] K. Delp, *Math Horizons* **20**, 5 (2012).
- [14] Y. Klett and K. Drechsler, in *Origami<sup>5</sup>*, edited by P. Wang-Iverson, R. J. Lang, and M. Yim (CRC Press, Boca Raton, FL, 2011), pp. 305–322.
- [15] K. Kuribayashi, K. Tsuchiya, Z. You, D. Tomus, M. Umemoto, T. Ito, and M. Sasaki, *Mater. Sci. Eng.* **419**, 131 (2006).
- [16] K. Miura, in *Proceedings of the 31st Congress of the International Astronautical Federation* (American Institute of Aeronautics and Astronautics, New York, 1980), pp. 1–10.
- [17] K. Miura, *Inst. Space Astronaut. Sci. Rep.* **618**, 1 (1985).
- [18] K. Miura, in *Research of Pattern Formation*, edited by R. Takaki (KTK Scientific Publishers, Tokyo, 1994), pp. 77–90.
- [19] P. Gruber, S. Häuplik, B. Imhof, K. Özdemir, R. Waclavicek, and M. A. Perino, *Acta Astronaut.* **61**, 484 (2007).
- [20] M. Schenk, A. D. Viquerat, K. A. Seffen, and S. D. Guest, *J. Spacecraft Rocket.* **51**, 772 (2014).
- [21] B. Thiria and M. Adda-Bedia, *Phys. Rev. Lett.* **107**, 025506 (2011).
- [22] F. Lechenault, B. Thiria, and M. Adda-Bedia, *Phys. Rev. Lett.* **112**, 244301 (2014).
- [23] T. Tachi, *J. Mech. Design* **135**, 111006 (2013).
- [24] S. Deboeuf, E. Katzav, A. Boudaoud, D. Bonn, and M. Adda-Bedia, *Phys. Rev. Lett.* **110**, 104301 (2013).
- [25] M. A. Dias and B. Audoly, *J. Mech. Phys. Solids* **62**, 57 (2014).
- [26] D. A. Huffman, *IEEE Trans. Comput.* **C-25**, 1010 (1976).
- [27] G. T. Pickett, *Europhys. Lett.* **78**, 48003 (2007).
- [28] M. Schenk and S. D. Guest, in *Origami<sup>5</sup>*, edited by P. Wang-Iverson, R. J. Lang, and M. Yim, (CRC Press, Boca Raton, FL, 2011), pp. 291–303.
- [29] A. A. Evans, J. L. Silverberg, and C. D. Santangelo, *Phys. Rev. E* **92**, 013205 (2015).
- [30] B. H. Hanna, J. M. Lund, R. J. Lang, S. P. Magleby, and L. L. Howell, *Smart Mater. Struct.* **23**, 094009 (2014).

- [31] V. Brunck, Origami Mechanics, Master's thesis, UPMC Université Paris 06, 2015.
- [32] S. Chaïeb, F. Melo, and J.-C. Gémard, *Phys. Rev. Lett.* **80**, 2354 (1998).
- [33] M. Ben Amar and F. Jia, *Proc. Natl. Acad. Sci. USA* **110**, 10525 (2013).
- [34] N. Bowden, S. Brittain, A. G. Evans, J. W. Hutchinson, and G. M. Whitesides, *Nature* **393**, 146 (1998).
- [35] C. Berge, *Graphs and Hypergraphs* (North-Holland, Amsterdam, 1973).
- [36] M. A. Dias, L. H. Dudte, L. Mahadevan, and C. D. Santangelo, *Phys. Rev. Lett.* **109**, 114301 (2012).